Dual-Satellite Stereoscopic Retrieval of Cloud Top Height Using *FY-4A* and *FY-4B*

Xiaotong HUANG[1,2,3], Yilun CHEN[1,2*], and Puxi LI[3]

1 *Key Laboratory of Tropical Atmosphere–Ocean System of Ministry of Education*, *School of Atmospheric Sciences*,
Sun Yat-sen University, *Zhuhai* 519080
2 *Southern Marine Science and Engineering Guangdong Laboratory (Zhuhai)*, *Zhuhai* 519080
3 *State Key Laboratory of Severe Weather*, *Chinese Academy of Meteorological Sciences*, *China Meteorological Administration*, *Beijing* 100081

(Received 29 March 2024; in final form 26 September 2024)

ABSTRACT

We developed a dual-satellite stereoscopic cloud top height (CTH) retrieval algorithm based on the visible band (0.65 μm) data of *Fengyun-4A* (*FY-4A*) and *FY-4B*. This algorithm offers an extensive longitude coverage from 55°E to 177°W. The analysis of system error based on error theory shows that the CTH we retrieved has an accuracy of 0.20–0.88 km and an uncertainty of 0.24–1.08 km over the entire area. The space resolution of the CTH we retrieved reached less than 0.005°. We conducted a CTH retrieval experiment and proceeded to compare our results with *FY-4B*'s CTH product and the Cloud–Aerosol Lidar and Infrared Pathfinder Satellite Observations (CALIPSO). Compared to CALIPSO, the CTH we retrieved has a bias of −2.4 km and the correlation coefficient is 0.80. In general, two next-generation geostationary satellites were used simultaneously to retrieve the CTH in our study, demonstrating the ability of this satellite combination to obtain better-quality CTH products by stereoscopic retrieval.

Key words: cloud top height (CTH), geostationary satellites, stereoscopic, Fengyun-4

Citation: Huang, X. T., Y. L. Chen, and P. X. Li, 2024: Dual-satellite stereoscopic retrieval of cloud top height using *FY-4A* and *FY-4B*. *J. Meteor. Res.*, **38**(6), 1141–1149, doi: 10.1007/s13351-024-4050-9.

1. Introduction

Clouds play an essential role in the earth's water and energy cycle through processes such as water vapor transport and radiation. One key cloud property that significantly impacts the calculation of cloud radiation forcing, also essential for understanding global warming, is cloud top height (CTH) (Zelinka et al., 2017; Zhuge et al., 2024). Eyre et al. (2022) pointed out that CTH and other cloud properties at different altitudes are crucial variables for assimilation in numerical weather prediction (NWP) models. Hence, there is a need for a high-quality CTH product that offers improved spatial coverage and temporal continuity to enhance NWP simulation capabilities and provide a better understanding of climate change.

Currently, the highest accuracy in CTH retrieval from satellite data is achieved through space-borne lidar, which is widely considered as the benchmark for assessing other approaches (Di Michele et al., 2013). In addition to lidar, single-satellite stereoscopic retrieval by Marchand et al. (2007) and O_2-A band absorption methods by Naud et al. (2007) have also been demonstrated the capability to generate high-quality CTH products. However, these approaches are limited to low-orbit satellites, resulting in observations of a specific location no more than twice a day. To overcome this limitation and attain better spatial and temporal coverage, geostationary satellite CTH products have been developed (Zhuge et al., 2021).

The most commonly used approach involves inferring cloud top temperature based on infrared channels and determining CTH using the temperature profile. However, the cloud-top temperature has a deviation from the ambient temperature, which is against the basic assumption of this method, leading to errors. Another widely studied technique is the infrared split-window method (Hamada and Nishi, 2010), which currently achieved the highest

---

Supported by the National Natural Science Foundation of China (42105068) and Innovation Group Project of Southern Marine Science and Engineering Guangdong Laboratory (Zhuhai) (311022006).

*Corresponding author: chenylun3@mail.sysu.edu.cn

accuracy of less than 1 km for high clouds. Chang et al. (2010) introduced the bi-channel CO_2-slicing technique to geostationary satellites, achieving a mean CTH lower than that of the Cloud–Aerosol Lidar with Orthogonal Polarization (CALIOP) by approximately 1 km.

In contrast to the aforementioned methods, the stereoscopic approach is based on stereoscopic geometry theory, utilizing multiple angles of observation to determine CTH. This method does not rely on radiation transmission physical models, thereby eliminating the influence of theoretical model defects on the results. Hasler (1981) made the first attempt in the 1980s, while the advent of next-generation geostationary satellites now provides high-resolution data, enabling stereo CTH to achieve higher accuracy and resolution.

The Fengyun-4 (FY-4) series satellites are China's next-generation geostationary quantitative remote sensing meteorological satellites (Zhu et al., 2023). *FY-4A* was launched in December 2016 and became operational in September 2017. Following suit, *FY-4B* was launched in June 2021 and underwent trial operation in June 2022, officially commencing its operations in December 2022. The *FY-4A* and *FY-4B* sub-satellite points are situated at 104.7° and 133.0°E, respectively. In March 2024, *FY-4B* was repositioned to 105.0°E, and *FY-4A* was repositioned to 86.5°E and stopped operational service. Both satellites are equipped with advanced geostationary orbit radiation imagers (AGRI) and share similar channel settings (Li et al., 2023; Liu et al., 2023). The highest resolution of 0.5 km is provided by the 0.65-μm visible band. Both *FY-4A* and *FY-4B* complete one full disk observation in 15 min, enabling them to retrieve near-synchronized full disk images up to 39 times a day.

In this study, we developed a CTH retrieval algorithm utilizing the 0.65-μm visible band reflectance from both *FY-4A* and *FY-4B* satellites based on stereoscopic theory. In Section 2, we explain thoroughly how the retrieval is conducted, and analyze the system bias according to error theory. Then in Section 3, we present the result of our retrieval experiment; also, to assess the feasibility of our algorithm, we conduct a comparative assessment of the retrieved CTH against the *FY-4B* CTH product (Tan et al., 2019) and CALIPSO CTH product. Finally, we conclude our study in Section 4.

2. Methods

2.1 *Stereoscopic theory*

Stereoscopic observation is a kind of approach that requires two satellites to observe the same cloud from different viewing angles, as depicted by Fig. 1a. Both satellites captured the cloud, but when observed by only one satellite, *FY-4A* for instance, the position of the cloud is located more to the east (the right-hand-side dashed cloud in Fig. 1a). When no radiative transfer method is considered, it is hard to determine the precise position of the cloud along the propagation path. However, by including an additional observation from another angle (*FY-4B*), we have another position of the cloud (the left-hand-side dashed cloud in Fig. 1a), together the real position of the cloud, both horizontally and vertically, can be calculated once we match the cloud features from two satellite images and identify the same cloud.

Figure 1b illustrates the geometric model for the single-satellite scenario, where equations can be formulated to represent the relationships among the satellite, cloud, and its projection (see Appendix A). By combining the equations for two satellites, we can solve them by iteration to obtain the real space location of the cloud. As the reflectance image depicts the characteristics of the cloud top and image matching relies on these features, the cloud height obtained theoretically corresponds to the cloud top height (CTH). However, there are instances where the image fails to accurately represent the features

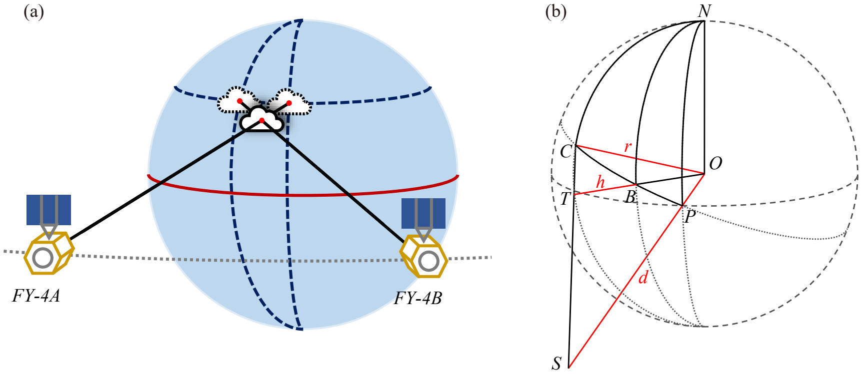

Fig. 1. (a) Schematic diagram and (b) geometric model of stereoscopic observation of cloud top height (CTH).

of the cloud top. For example, visible channels may be insensitive to thin ice clouds above thick clouds, also water vapor absorption channels are insensitive to middle and low clouds. In such cases, improvements to the stereoscopic observation method, such as incorporating an additional channel, may be necessary to obtain the true CTH.

In our study, the choice of combination of *FY-4A* and *FY-4B* has multiple advantages. According to stereoscopic theory, when the two satellites are sitting close to each other, their angle of view becomes similar, so the vertical feature of the cloud becomes hard to depict by two images, that is, the vertical accuracy is affected. On the other hand, when the two satellites are sitting far from each other, the vertical features of clouds can be better depicted by different views of observation; however, the image grid becomes coarse near the edge of both satellite's images, which affect the vertical resolution of CTH product from another aspect. Moreover, when the two satellites are too far from each other, the overlap range of their image becomes small and affects the space range of the stereoscopic CTH product. Hasler (1981) pointed out that around 30° of sub-satellite point difference is the most ideal distance for stereoscopic retrieval. In our case, *FY-4A* and *FY-4B* have a longitudinal difference of 28.3° between their locations above the equator, which is highly suitable for performing stereoscopic retrieval. Another advantage of this combination is that they belong to the same series of geostationary satellites and they carry the same imager instrument onboard, so the data consistency is very good.

2.2 *FY-4A and FY-4B retrieval algorithms*

In Fig. 2, the process of our algorithm is illustrated, which consists of four main steps: remapping, matching, geolocation correction, and solving geometric equations.

The first step is to define the targeted area within the retrievable range. We extract the images of the targeted area from both satellites' full disk images and proceed to remap the image. We use the grid of whichever satellite is closest to the targeted area. For instance, if the targeted area is located more to the east, then we use *FY-4B*'s grid, and then we remap the other satellite's image (*FY-4A*) onto this grid by near-point searching. This operation aims to mitigate distortions caused by variations in observation angles. Next, we look for identical cloud projection points from two images through matching. A small square (20 by 20 pixels) is selected in one image,

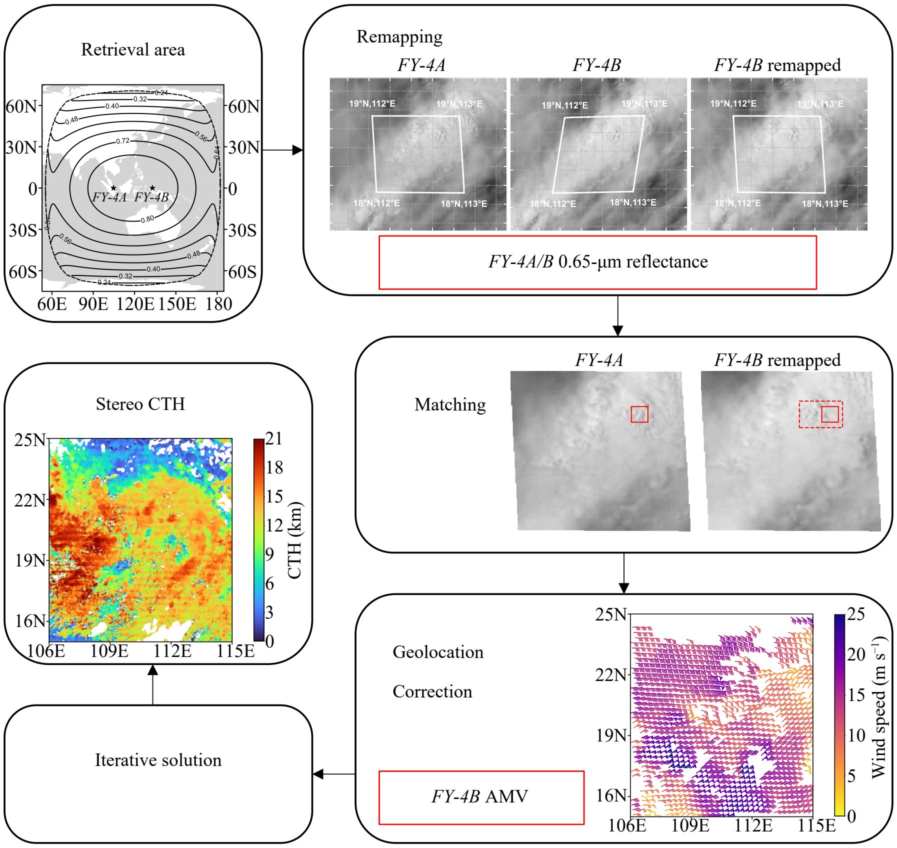

Fig. 2. Flowchart for *FY-4A* and *FY-4B* stereoscopic CTH retrieval algorithm. AMV: atmosphere motion vector.

and we move a square of the same size in the other image within a calculated search range until the correlation coefficient of two square images reaches the highest. In our experiments, the average matching correlation coefficient was 0.86, with a median of 0.91. The central locations of both squares are then recorded as matched projection points on a cloud top. The matching process is again conducted with two satellites switched around, ensuring a one-to-one correspondence.

Because *FY-4A* and *FY-4B* have different viewing angles and scanning patterns, we then correct bias brought by the observation time difference. The CTH bias can grow up to 3 km when no correction is applied, which is hard to ignore. To solve this time-alignment problem, we use the scan time provided by both satellites' level 1 data and the FY-4 atmosphere motion vector (AMV) product (Chen et al., 2020). During application, we found that both data do not have enough accuracy for correction, so we applied an composed approach to better use the two products. The details of this operation can be found in Appendix C.

To calculate the CTH, we established geometric equations based on the relationship between the satellites and the earth (detailed in Appendix A). By utilizing the matched pairs' coordinates, and satellite and earth parameters, we solved these equations by iterations to retrieve the CTH and sub-cloud point coordinates. Finally, we eliminate unreasonable results as quality control for the CTH product. To be specific, we eliminate too high (more than 20 km) or too low (less than 0 km) CTHs, and results that deviate significantly from surrounding CTH results are also eliminated.

2.3 *Quality assessment*

Our CTH retrieval algorithm's reliability is evaluated by the uncertainty and accuracy. The calculation of uncertainty is based on error analysis theory, while the calculation of accuracy is aimed at comparing our algorithm with previous studies. A description of error factors considered in the process and step details can be found in Appendix B.

The vertical accuracy of our CTH retrieval algorithm ranges from 0.20 to 0.88 km, while the expanded uncertainty ranges from 0.24 to 1.08 km. This result aligns with previous research findings. Lee et al. (2020) presented the theoretical accuracy of various geostationary satellite combinations for stereoscopic observation in Asia, stating that the combination of *FY-4A* and *Himawari-8* should achieve the highest accuracy of 0.69 km. Carr et al. (2020) employed the *GOES-16/17* combination for stereoscopic observation with a theoretical accuracy of 343 m. The theoretical accuracy of CTH retrieval using Multiangle Imaging Spectroradiometer (MISR) with an image resolution of 1.1 km is 562 m, which can be further improved to 275 m by employing a larger angle camera (Moroney et al., 2002). Thanks to the advances in the horizontal resolution of next-generation geostationary satellite imagers, the accuracy of retrieving CTH by stereoscopic approaches has reached the same level as low-orbit satellites.

The coverage of the *FY-4A* and *FY-4B* combination for CTH retrieval encompasses East Asia, South Asia, the eastern Indian Ocean, the western Pacific Ocean, and maritime continents, promising a potential to provide high-precision CTH products with broad spatial coverage, high accuracy, reliable temporal continuity, and improved horizontal resolution for the Asian monsoon region.

3. Experimental results

We conducted a CTH retrieval experiment using our algorithm. The selected date is 10 August 2022, with a 10 by 9 degrees square area located 15°–25°N, 106°–115°E. The main weather system inside the observing range is Tropical Cyclone (TC) Mulan. The TC cloud system is a complex of convective clouds, outflow thin cirrus, and lower rain clouds in weak precipitation zones. Such diversity offered ideal conditions for the performance evaluation of our CTH retrieval algorithm.

The full disk observations of *FY-4A* and *FY-4B* were conducted from 0700 to 0715 UTC, during which the CALIPSO passed over the experiment area from south to north along a trajectory of 15.00°N, 113.97°E to 25.00°N, 111.63°E from 0710:10 to 0712:55 UTC. CALIPSO is a low-orbit satellite within the A-train constellation carrying the Cloud–Aerosol Lidar with Orthogonal Polarization (CALIOP). Two CALIPSO data products were included for the assessment: the 532-nm total backscattering coefficient (level 1) and the CTH product (level 2). The positions of *FY-4A* and *FY-4B* are 104.7° and 133.0°E for the data used here.

Figure 3 presents three selected partial areas of this CTH retrieval experiment. The three columns in Fig. 3 depict the visible channel (0.65 μm) image of *FY-4B*, the retrieved CTH by our algorithm, and the CTH product of *FY-4B*, respectively. The main cloud structure in the first row of Fig. 3 is part of an outer spiral rain-band of the TC, located southeast of the TC center. In the second row of Fig. 3, we select an area located northeast of the TC center, on the path of the TC movement, mostly high clouds of the TC's eyewall. In the third row of Fig. 3, we

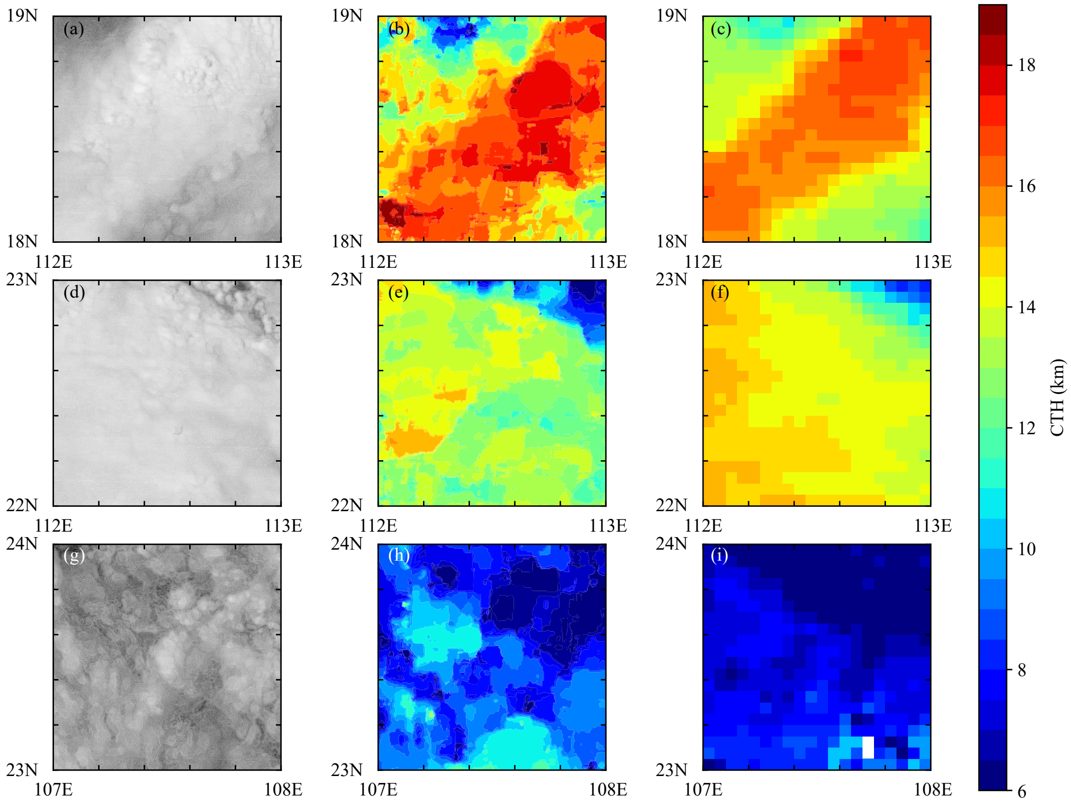

Fig. 3. The three 1° × 1° areas taken out of the CTH retrieval experiment by three rows, which are located over (a–c) 18°–19°N, 112°–113°E, (d–f) 22°–23°N, 112°–113°E, and (g–i) 23°–24°N, 107°–108°E. The first column (a, d, g) presents the visible channel (0.65 μm) reflectance image by *FY-4B*. The second column (b, e, h) presents the stereoscopic algorithm retrieved CTH. The third column (c, f, i) presents the *FY-4B* CTH product.

select an area located northwest of the TC center, where low rain clouds above land occupy. The three areas with distinct cloud features offer a clear view of how our retrieval algorithm performed over multiple conditions.

In Fig. 3a, an overshooting top can be observed at approximately 18.75°N, 112.55°E. The local time (LT) was 1500 LT, so the sun was positioned west, making a step-like shadow evident on the east side. The corresponding position in Fig. 3b is at approximately 18.65°N, 112.60°E. The differences in longitude and latitude of these two points are approximately 0.05° and 0.1°, respectively, which is due to the correction of the sub-cloud point during the retrieval by our algorithm. In comparison to Fig. 3b, the CTH product of *FY-4B* shown in Fig. 3c exhibits limitations in accurately capturing the detailed features of the overshooting tops. This improvement in observing overshooting tops from geostationary satellites may promote the data quality used in TC overshooting tops research (Sun et al., 2017).

Within a small area of 18.8°–19.0°N, 112.2°–112.6°E, the *FY-4B* CTH product exhibits a vertical drop of more than 6 km when compared to the convective clouds in the rain-band. The CTH retrieved by our algorithm verified this feature and displayed it clearly as shown in Fig. 3b. This discrepancy is highlighted by the findings of Houze (2010), who noted the presence of a unique structure in the convective tops of spiral rain-bands, particularly a strong descending airflow near the eyewall on the inner edge of the rain-band. A similar structure can also be found in Figs. 3d, e where most clouds are part of the eyewall with its edge on the northeast corner. Our algorithm again captured the CTH vertical drop feature more clearly compared to the *FY-4B* CTH product (Fig. 3f).

In the rain clouds zone shown by Figs. 3g–i, the convective characteristic is captured closely by stereoscopic retrieval while missed out by the *FY-4B* product, concluded from comparison between Figs. 3h and 3i. We are confident about the convective structure because according to Fig. 3g: there are contrasts in reflectance distribution indicating the dispersed distribution of low convective rains, and therefore, indicating a diversity in CTH. It should be noted that the cloud positions are variant between Figs. 3g and 3h as a result of the stereoscopic observation effect, and that *FY-4B* reflectance is observed from an eastern view while stereoscopic retrieval shows the real position of the clouds.

Figure 4a presents the overall statistical distribution of

CTH retrieved by our algorithm along with that of the *FY-4B* product. The interval is set to 0.5 km, and the vertical axis represents probability density. The CTH retrieved by our algorithm shows a trimodal structure. The 2-km peak is distributed in the weak precipitation area north of the TC center above land. The peak at 7–8 km corresponds to the tropical middle layer discovered by Riley and Mapes (2009). The 14-km peak corresponds to the convective clouds in the TC spiral rain-bands with the 8-km peak located in the sinking area between the spiral rain-bands. The *FY-4B* CTH product distribution exhibits a simpler bimodal structure. The 13-km peak is contributed by the TC spiral cloud system, while the 6-km peak is attributed to the cloud system above land north of the TC center. The distribution difference is also shown in Fig. 4b, a frequency distribution of CTH bias between CTH retrieved by our algorithm and the *FY-4B* product. To confirm the resolution difference between the two products, the *FY-4B* product was downscaled by using near-point searching to match the sample size of stereoscopic retrieval. Note that there is a field of view deviation between the stereoscopic retrieval and the *FY-4B* product, which may slightly impact the results of the correlation analysis. The CTH retrieved by our stereoscopic algorithm, exhibits a height difference of 0.45 km higher than the *FY-4B* product on average, and the correlation coefficient between them is 0.69. Similar to the comparison result between *FY-4A* and Moderate-resolution Imaging Spectroradiometer (MODIS) CTH products (Zhang et al., 2022), the *FY-4B* CTH product overestimates the CTH of low clouds and underestimates the CTH of high clouds.

Figure 4c compares the CTH of CALIPSO product, stereoscopic retrieval, and *FY-4B* product. The CTH of the CALIPSO product remains highest from 15° to 23°N indicating the TC cloud system. The *FY-4B* product is lower than CALIPSO by 1.46 km overall, while for stereoscopic retrieval it is 2.40 km. Lee et al. (2020) conducted stereoscopic CTH retrieval experiments using Cloud Profiling Radar (CPR) data as examination, reporting a deviation ranging from −0.25 to 0.5 km. Lee and Shin (2021) conducted another examination using CALIPSO data and the deviation was approximately −2 km, which is similar to our result.

Except for two overshooting tops located near 17.5° and 19°N in Fig. 4c, the CTH retrieved by our algorithm falls between CALIPSO and *FY-4B* product to the south of 19°N, and lower than both products to the north of 19°N. This disparity can be attributed to the slightly uneven observation time difference between the two satellites in the experiment area. Wylie et al. (1998) suggested that the low CTH retrieved by the stereoscopic approach is because the reflectance captured by the radiation imager predominantly represents scattering within the cloud rather than from the cloud top. Therefore, an improvement for better quality of the CTH retrieved is to

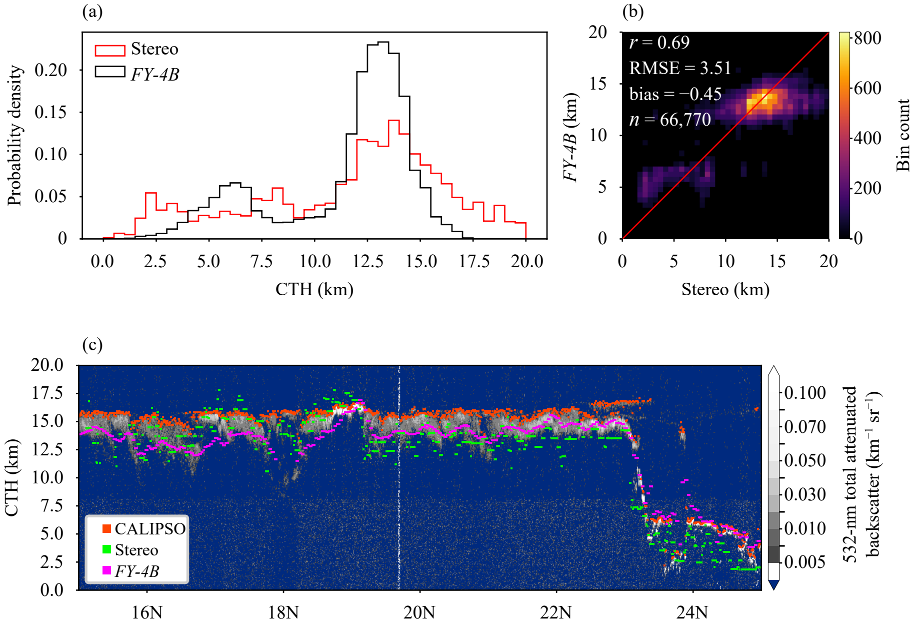

Fig. 4. (a) Distribution of CTH retrieved by the stereoscopic algorithm and *FY-4B* CTH product and (b) their correlation distribution frequency, where bin counts represent the sample point counts within the grid, with intervals of 0.5 km and total sample size of 66,770 points. (c) Vertical CTH scatterplot of the CALIPSO product, our algorithm, and the *FY-4B* product, with 532-nm total attenuated backscatter detected by CALIOP onboard CALIPSO as background.

combine features shown by different channels, such as merging the visible channel with the infrared channel (Lee and Shin, 2021).

4. Conclusions

In this study, we have developed an algorithm for retrieving CTH based on stereoscopic theory, utilizing the high-resolution capabilities of China's next-generation geostationary satellites, *FY-4A* and *FY-4B*.

We have provided theoretically calculated accuracy and uncertainty, with a retrieval experiment to assess the algorithm's performance. The retrieved CTH data from these geostationary satellites offer broad spatial and temporal coverage with ideal horizontal resolution, suggesting the potential to significantly contribute to the studies of weather system evolution, particularly within the Asian monsoon region.

Additionally, it can be integrated with other variables, such as AMV, to enhance the quality of current results. Future enhancements to the algorithm will focus on refining time difference correction and increasing its overall reliability.

Acknowledgments. The CALIPSO product data were downloaded from the Atmospheric Science Data Center at NASA Langley Research Center of the United States (https://asdc.larc.nasa.gov/project/CALIPSO).

Appendix A: Geometry equations

The geometry model for a single satellite is illustrated by Fig. 1b, assuming the targeted cloud top is at a fixed point T with its height as CTH. The letters O, N, S, C, P, and B represent the center of the earth, the geographic North Pole, the satellite radiation imager, projection of the cloud, the sub-satellite point, and the sub-cloud point, respectively. Also r and d represent the radius of the earth and satellite orbit. Assuming that the earth is a sphere and ignoring the influence of atmospheric refraction on the propagation path, a set of equations describing the relationship between the satellite radiation imager, the cloud, and its projection can be written as follows. The arc mark denotes center angle, for instance, $\overset{\frown}{\mathrm{CN}}$ means $\angle$CON.

$$\frac{\sin(\angle \mathrm{CPN})}{\sin\left(\overset{\frown}{\mathrm{CN}}\right)} = \frac{\sin(\angle \mathrm{PCN})}{\sin\left(\overset{\frown}{\mathrm{PN}}\right)}, \tag{A1}$$

$$\frac{\sin(\angle \mathrm{PNC})}{\sin\left(\overset{\frown}{\mathrm{PC}}\right)} = \frac{\sin(\angle \mathrm{PCN})}{\sin\left(\overset{\frown}{\mathrm{PN}}\right)}, \tag{A2}$$

$$\cos\left(\overset{\frown}{\mathrm{CN}}\right) = \cos\left(\overset{\frown}{\mathrm{PN}}\right)\cos\left(\overset{\frown}{\mathrm{PC}}\right) + \sin\left(\overset{\frown}{\mathrm{PN}}\right)\sin\left(\overset{\frown}{\mathrm{PC}}\right)\cos(\angle \mathrm{CPN}), \tag{A3}$$

$$\frac{r}{\sin(\angle S)} = \frac{d}{\sin(\angle \mathrm{OCS})}, \tag{A4}$$

$$\frac{\sin(\angle \mathrm{PNB})}{\sin\left(\overset{\frown}{\mathrm{PB}}\right)} = \frac{\sin(\angle \mathrm{BPN})}{\sin\left(\overset{\frown}{\mathrm{BN}}\right)}, \tag{A5}$$

$$\cos\left(\overset{\frown}{\mathrm{PB}}\right) = \cos\left(\overset{\frown}{\mathrm{PN}}\right)\cos\left(\overset{\frown}{\mathrm{BN}}\right) + \sin\left(\overset{\frown}{\mathrm{PN}}\right)\sin\left(\overset{\frown}{\mathrm{BN}}\right)\cos(\angle \mathrm{PNB}), \tag{A6}$$

$$\frac{\mathrm{CTH} + r}{\sin(\angle S)} = \frac{d}{\sin(\angle \mathrm{OTS})}. \tag{A7}$$

CTH cannot be retrieved by single satellite because there are 8 unknown variables ($\angle$CPN, $\angle$PCN, $\overset{\frown}{\mathrm{PC}}$, $\overset{\frown}{\mathrm{PB}}$, $\angle S$, $\angle$BPN, $\overset{\frown}{\mathrm{BN}}$, and CTH) and 7 equations. When using two satellites, the same set of equations can be established for the other satellite, where CTH, points B and T remain constant. Thereupon, a total of 14 equations can be written, with 13 unknown variables (CTH, $\angle$BPN, $\overset{\frown}{\mathrm{BN}}$, and five variables for each satellites: $\angle$CPN, $\angle$PCN, $\overset{\frown}{\mathrm{PC}}$, $\overset{\frown}{\mathrm{PB}}$, and $\angle S$). Thus, we can retrieve CTH by solving the equation set.

Known variables include the physical parameters of the earth (r), the satellite parameters (d and point P), and the geolocations of the projections of the cloud (point C). Equations (A1)–(A6) for each satellite constitute the first 12 equations, from which the first 12 unknown variables can be solved, including $\angle$CPN, $\angle$PCN, $\overset{\frown}{\mathrm{PC}}$, $\overset{\frown}{\mathrm{PB}}$, and $\angle S$ for the two satellites, as well as the sub-cloud point (point B), longitude of which is related to the sub-satellite point and $\angle$BPN, and latitude of which is related to $\overset{\frown}{\mathrm{BN}}$. Equation (A7) for each satellite solves the CTH as the both-used side of two different known triangles. To reduce rounding errors, the average of the CTH obtained by solving two equations separately is calculated. Before giving a final result of the CTH and sub-cloud point, quality control is performed to filter negative and excessive CTHs, which are generated mainly due to errors in the image-matching step as a result of multi-layer clouds or deformed cloud features observed from different angles.

Appendix B: Error analysis calculation

The uncertainty represents the quality of the CTH we retrieved, the calculation of which has considered all possible errors in the steps depicted in Fig. 2. Followings are the detailed descriptions.

During remapping, multiple sources of error eventually result in loss or distortion of cloud top features, including the differences between the two satellites' calibrations of the reflectance image, zenith angle, observation time, and directions, also the usage of near point searching method and the presence of multilayer clouds. The errors in the matching step can be introduced from quality-lowered cloud top features, and also from the disposition of the targeted cloud points, which may not fall precisely at the center of the window region. These errors are collectively reflected in the offset of projection coordinates on the grid.

The FY-4 AMV product used in geolocation correction introduced most errors. The wind speed and direction have deviations from actual values due to the AMV product's generation time and algorithm. During the specific correction processing, all the errors (including the ones introduced by our algorithm) are eventually corrected to the longitude dimension.

In the final step, the error in CTH is transferred from all the input variables through the equations. Errors introduced by the geometry model, the radius of the earth, and satellite orbits are not considered because they have been calibrated when retrieved. Errors introduced by sub-satellite point shifts are eventually reflected in the shift of projection points through the equations. To sum that up, the only error influencing CTH that requires calculation is in the projection points coordinates' longitudes, so we only consider longitude deviations when calculating the composite uncertainty of the CTH.

The formulas of uncertainty calculation are shown below, where h, $\mathrm{lon_a}$, and $\mathrm{lon_b}$ represent the CTH, longitudes of the projection points of *FY-4A* and *FY-4B,* respectively. The standard uncertainties introduced by the longitude deviations of the two projection points, $u_{\mathrm{lon_a}}$ and $u_{\mathrm{lon_b}}$, are B-class evaluated. Within the range of $(\mathrm{lon_b} - \delta\mathrm{lon_b}, \mathrm{lon_b} + \delta\mathrm{lon_b})$ the uncertainty on the longitude dimension is determined by the triangular distribution, with the inclusion factor $k = \sqrt{6}$ [Eq. (B1)]. The error coefficient between the CTH and the longitude of the projection points is obtained numerically based on the geometric equations. The combined standard uncertainty of the CTH (u_h) is obtained by Eq. (B2), where we take 2 as the inclusion factor K. The extended uncertainty U_h, which is the uncertainty expressing the error range finally, is then obtained by Eq. (B3).

$$u_{\mathrm{lon}_i} = \frac{\delta\mathrm{lon}_i}{k}\left(i = \mathrm{a},\ \mathrm{b},\ k = \sqrt{6}\right), \tag{B1}$$

$$u_h = \sqrt{\left(\frac{\partial h}{\partial \mathrm{lon_a}}\right)^2 u^2_{\mathrm{lon_a}} + \left(\frac{\partial h}{\partial \mathrm{lon_b}}\right)^2 u^2_{\mathrm{lon_b}}}, \tag{B2}$$

$$U_h = K \cdot u_h,\ K = 2. \tag{B3}$$

In addition to the extended uncertainty, we also calculated the vertical accuracy of the CTH [Eq. (B4)]. The accuracy is defined as the deviation in CTH vertically caused by the longitude deviation of one grid point on the reflectance image grid. When calculating, we considered the grid size distribution difference between *FY-4A* and *FY-4B*, which is significant at the eastern and western edges of the valid area range.

$$\delta h = \left(\frac{\partial h}{\partial \mathrm{lon_a}}\delta\mathrm{lon_a} + \frac{\partial h}{\partial \mathrm{lon_b}}\delta\mathrm{lon_b}\right)/2. \tag{B4}$$

Appendix C: Time-alignment

For each point, we calculate the time difference between two satellites' level 1 data, and multiply with the AMV product to see how long distance the cloud has shifted. But we found that the level 1 data and the AMV product don't have enough accuracy for subtle changes to eliminate the bias as we expected. Therefore, we correct the AMV product first for this step.

First, we assume the time difference is the same over a certain range (in this experimental case, a 10 by 9 degrees square area). Then for each matched point pair, we calculated a value (w_0) presenting the time difference derived from their latitude difference and wind speed's latitudinal projection provided by the FY-4 AMV product. The theoretical basis is that both geostationary satellites sit above the equator, so there should not be a deviation of view on the latitudes of the same cloud. In reality, the sub-satellite point shift in 0.5° range, according to the geometry equations, this shift has minor effect in this step compared to other factors. However, the distribution of w_0 is uneven over the selected area, indicating the AMV product has deviations from the true wind field. To address this issue, we use the mean value of w_0 over the selected area and our assumption of same time difference to correct the wind field first, and then based on this corrected wind field, we calculate the longitude difference ought to be added or subtracted for each matched point pairs to complete this step of correction eliminating time alignment issues.

REFERENCES

Carr, J. L., D. L. Wu, J. Daniels, et al., 2020: GEO–GEO stereo-tracking of atmospheric motion vectors (AMVs) from the geostationary ring. *Remote Sens.*, **12**, 3779, doi: 10.3390/rs12223779.

Chang, F.-L., P. Minnis, B. Lin, et al., 2010: A modified method for inferring upper troposphere cloud top height using the GOES 12 imager 10.7 and 13.3 μm data. *J. Geophys. Res. At-*

mos., **115**, D06208, doi: 10.1029/2009JD012304.

Chen, Y. D., J. Shen, S. Y. Fan, et al., 2020: Characteristics of *Fengyun-4A* satellite atmospheric motion vectors and their impacts on data assimilation. *Adv. Atmos. Sci.*, **37**, 1222–1238, doi: 10.1007/s00376-020-0080-0.

Di Michele, S., T. McNally, P. Bauer, et al., 2013: Quality assessment of cloud-top height estimates from satellite IR radiances using the CALIPSO lidar. *IEEE Trans. Geosci. Remote Sens.*, **51**, 2454–2464, doi: 10.1109/TGRS.2012.2210721.

Eyre, J. R., W. Bell, J. Cotton, et al., 2022: Assimilation of satellite data in numerical weather prediction. Part II: Recent years. *Quart. J. Roy. Meteor. Soc.*, **148**, 521–556, doi: 10.1002/qj.4228.

Hamada, A., and N. Nishi, 2010: Development of a cloud-top height estimation method by geostationary satellite split-window measurements trained with *CloudSat* data. *J. Appl. Meteor. Climatol.*, **49**, 2035–2049, doi: 10.1175/2010JAMC2287.1.

Hasler, A. F., 1981: Stereographic observations from geosynchronous satellites: An important new tool for the atmospheric sciences. *Bull. Amer. Meteor. Soc.*, **62**, 194–212, doi: 10.1175/1520-0477(1981)062<0194:SOFGSA>2.0.CO;2.

Houze, R. A. Jr., 2010: Clouds in tropical cyclones. *Mon. Wea. Rev.*, **138**, 293–344, doi: 10.1175/2009MWR2989.1.

Lee, J., D.-B. Shin, C.-Y. Chung, et al., 2020: A cloud top-height retrieval algorithm using simultaneous observations from the *Himawari-8* and FY-2E satellites. *Remote Sens.*, **12**, 1953, doi: 10.3390/rs12121953.

Lee, J.-H., and D.-B. Shin, 2021: Algorithm for improved stereoscopic cloud-top height retrieval based on visible and infrared bands for *Himawari-8* and *FY-4A*. *Remote Sens.*, **13**, 4993, doi: 10.3390/rs13244993.

Li, S. Q., X. Z. Han, Y. P. Zhang, et al., 2023: First look of surface vegetation from the advanced geostationary radiation imager (AGRI) onboard *Fengyun-4B*. *J. Meteor. Res.*, **37**, 536–550, doi: 10.1007/s13351-023-3005-x.

Liu, C., Y. X. Song, G. N. Zhou, et al., 2023: A cloud optical and microphysical property product for the advanced geosynchronous radiation imager onboard China's *Fengyun-4* satellites: The first version. *Atmos. Oceanic Sci. Lett.*, **16**, 100337, doi: 10.1016/j.aosl.2023.100337.

Marchand, R. T., T. P. Ackerman, and C. Moroney, 2007: An assessment of multiangle imaging spectroradiometer (MISR) stereo-derived cloud top heights and cloud top winds using ground-based radar, lidar, and microwave radiometers. *J. Geophys. Res. Atmos.*, **112**, D06204, doi: 10.1029/2006JD007091.

Moroney, C., R. Davies, and J.-P. Muller, 2002: Operational retrieval of cloud-top heights using MISR data. *IEEE Trans. Geosci. Remote Sens.*, **40**, 1532–1540, doi: 10.1109/Tgrs.2002.801150.

Naud, C., K. L. Mitchell, J.-P. Muller, et al., 2007: Comparison between ATSR-2 stereo, MOS O_2-A band and ground-based cloud top heights. *Int. J. Remote Sens.*, **28**, 1969–1987, doi: 10.1080/01431160600641806.

Riley, E. M., and B. E. Mapes, 2009: Unexpected peak near −15°C in CloudSat echo top climatology. *Geophys. Res. Lett.*, **36**, L09819, doi: 10.1029/2009GL037558.

Sun, L. X., X. Y. Zhuge, and Y. Wang, 2017: Favorable environments for the occurrence of overshooting tops in tropical cyclones. *Adv. Atmos. Sci.*, **34**, 532–544, doi: 10.1007/s00376-016-6122-y.

Tan, Z. H., S. Ma, X. B. Zhao, et al., 2019: Evaluation of cloud top height retrievals from China's next-generation geostationary meteorological satellite *FY-4A*. *J. Meteor. Res.*, **33**, 553–562, doi: 10.1007/s13351-019-8123-0.

Wylie, D. P., D. Santek, and D. O. C. Starr, 1998: Cloud-top heights from *GOES-8* and *GOES-9* stereoscopic imagery. *J. Appl. Meteor. Climatol.*, **37**, 405–413, doi: 10.1175/1520-0450(1998)037<0405:CTHFGA>2.0.CO;2.

Zelinka, M. D., D. A. Randall, M. J. Webb, et al., 2017: Clearing clouds of uncertainty. *Nat. Climate Change*, **7**, 674–678, doi: 10.1038/nclimate3402.

Zhang, A. Q., Y. L. Chen, X. Pan, et al., 2022: Precipitation microphysics of tropical cyclones over Northeast China in 2020. *Remote Sens.*, **14**, 2188, doi: 10.3390/rs14092188.

Zhu, S. Y., Z. Q. Ma, S. L. Ren, et al., 2023: FPCI and SPCI are proposed to distinguish the frontal and saturated precipitation systems based on FY-4A. *IEEE Geosci. Remote Sens. Lett.*, **20**, 1000705, doi: 10.1109/LGRS.2023.3247755.

Zhuge, X. Y., X. L. Zou, and Y. Wang, 2021: AHI-derived daytime cloud optical/microphysical properties and their evaluations with the collection-6.1 MOD06 product. *IEEE Trans. Geosci. Remote Sens.*, **59**, 6431–6450, doi: 10.1109/TGRS.2020.3027017.

Zhuge, X. Y., X. L. Zou, L. Yu, et al., 2024: Introduction to the NJIAS *Himawari-8/9* cloud feature dataset for climate and typhoon research. *Earth Syst. Sci. Data.*, **16**, 1747–1769, doi: 10.5194/essd-16-1747-2024.

Tech & Copy Editor: Yuxiang ZHU